Academy journal for Basic and Applied Sciences (AJBAS) Volume 7 issue 1, 2025

Preparation and Characterization of Iron Titanate Nanoclusters

Abdussallam N. Eldewik, Hadeel A. Abduljawad. *Department of Chemistry,*
The Libyan Academy for Postgraduate Studies
Tripoli, Libya
beldewik@academy.edu.ly

***Abstract*—This work presents a quantitative investigation of the synthesis and characterization of iron, titanium, and mixed iron-titanium nano-clusters. Special attention is given to the hydrothermal synthesis of glutamic acid in organic media. The goal of this work is to create nanoparticles for use in larger-scale applications and to establish a new avenue of research into the synthesis and characterization of these particles. Several methods have been employed to characterize the nanoparticles, including scanning electron microscopy (SEM), energy dispersive X-ray (EDX), Fourier transform infrared spectroscopy (FT-IR), X-ray diffraction (XRD), thermogravimetric analysis (TGA), and diffuse reflectance UV-Vis spectroscopy.**

The results from these techniques confirmed the XRD findings, showing the formation of titanium oxide (anatase), iron oxide (hematite), and ilmenite nanoparticles. UV-Vis spectroscopy revealed that all of the product samples are semiconductors, and TGA validated their thermal stability.

Keywords—Hydrothermal synthesis, nano-clusters, Titanium oxide (Anatase), Iron oxide (Hematite), Ilmenite.

INTRODUCTION

Titanium and iron nanoparticles are produced with emphasis on these metals, as the transition metals of titanium and iron have numerous applications in electronics, construction, medicine, cosmetics, and sunscreens (Hussain et al., 2024). Glutamic acid, an amino acid, is a bio-based and environmentally friendly polymer material that is water-soluble and has high strength (Liu et al., 2023). Using glutamic acid and L-glutamine, ternary complexes of Cu (II), Co (II), Ni (II), and Fe (II) were formed. This amino acid's terminal C(=O)-NH_2 group allows it to form significant hydrogen bonds (Abdel-Rahman et al., 2017).

The thermal process has been implemented due to its ability to regulate the reaction, which in turn controls surface chemistry, crystalline phase, material size, and particle morphology, temperature, pressure, solution content, solvent characteristics, and additives. This method is advantageous because it enables the synthesis of a large number of nanoparticles (NPs) at a low cost. It is a straightforward and efficient technique for creating nanoparticles of various materials (Carp et al., 2004).

The formation of metal nanoparticles typically occurs on monometallic or bimetallic substrates. A monometallic nanoparticle consists of a single metal, which creates nanoparticles based on its unique physical characteristics. In recent years, bimetallic nanocrystals (NCs) have gained significant attention from scientists. Since the two metals work together, bimetallic nanocrystals are expected to exhibit superior physical and chemical properties compared to just a combination of two monometallic particles. Moreover, the characteristics of bimetallic nanocrystals are heavily influenced by their shape, structure, and atomic configuration. By effectively controlling these parameters, the functionality of these nanocrystals for specific applications can be enhanced, and their properties can be regulated (Li et al., 2021).

MATERIALS AND METHODS

MATERIALS

All chemicals used in preparation of resulted products are listed in Table 1.

Table 1: List of all chemicals used in this study.

Compound Name	Formula	Source
Iron (III) Chloride	$FeCl3$	Riedal-de Haen AG
Titanium (III) Chloride	$TiCl3$	Alfa Aesar Chemicals
Glutamic Acid (GLU)	$C5H9NO4$	Alfa Aesar UK
Dimythlformamide (DMF)	$C3H7NO$	Carlo Eerba. French

METHODS

Samples of titanium, iron, and their mixtures at different concentrations were prepared using the

DOI:10.5281/zenodo.15632026

same hydrothermal method: (Ti 100%, Fe 0%), (Ti 10%, Fe 80%), (Ti 30%, Fe 70%), (Ti 50%, Fe 50%), and (Ti 80%, Fe 20%). Each sample received 10 mL of DMF via pipette while being magnetically stirred at room temperature. After one hour of vigorous stirring, the pH of the resulting solution was measured; the findings are shown in Table 2 For all samples, the solution was transferred into a Teflon-lined stainless-steel autoclave and heated to 120°C for 24 hours in an oven. The precipitate was then allowed to cool to room temperature before being filtered and repeatedly rinsed with Di-ionized water to remove any remaining contaminants. The weight of the products was measured using a sensitive balance, and the weights are shown in Table 2.

Table 2: Weights and pH Values for the Product Samples

No. of Sample	**Percen-tage (%)**	**Vol. of Ti (ml)**	**Vol. of Fe (ml)**	**PH**	**Wight (gram)**
1	100	60	0	1.18	0.4
2	0	0	60	1.82	1
3	10	6	54	1.73	0.4
4	30	18	42	1.64	0.422
5	50	30	30	1.61	0.206
6	80	48	12	1.24	3

CHARACTERIZATION

The characterization of the nano-products was carried out using scanning electron microscopy (SEM), Fourier transform infrared spectroscopy (FTIR), thermogravimetric analysis (TGA), X-ray diffraction (XRD), energy-dispersive X-ray spectroscopy (EDX), and UV–Vis diffuse reflectance spectroscopy.

RESULTS AND DISCUSSION:

XRD ANALYSIS:

Figure 1 shows the XRD of samples 3, 4, and 5, with typical peaks at 2θ values of 24.27°, 33.18°, 35.76°, 49.58°, 54.06°, 57.58°, 62.56°, and 64.22°, which are comparable to the reported peaks in the 2θ region of ilmenite (23.97°, 33.04°, 35.67°, 40.90°, 49.32°, 53.76°, 57.09°, 62.36°, and 64.20°) that were reported by Morín et al. (2017). These results confirm that pure ilmenite ($FeTiO_3$) has a trigonal (hexagonal axes) crystal structure, according to JCPDS card no. 75-1207.

Due to its identical composition, sample 2 (0% Ti) was found to have the same XRD pattern as $FeTiO_3$, as shown in Figure 17. Fe_2O_3 has a hexagonal crystal structure made up of iron atoms encircled by six oxygen atoms, which is a trigonal-hexagonal scalenohedral structure with space group R3c. The lattice parameters are a = 5.0356 nm, c = 13.7489 nm, and the unit cell contains six formula units (Mirzaei et al., 2016)

Using the Debye-Scherrer equation, the average crystallite size is calculated:
□ = Kλ / βcosθ, where K is the shape factor (typically 0.89), λ is the wavelength of the incident beam, β is the wavelength of the diffraction line measured in radians at half maximum intensity (FWHM), θ is the Bragg angle, and D is the crystallite diameter (He et al., 2008).

When a diffraction pattern is indexed, the proper Miller indices are assigned to each peak (reflection). The XRD pattern is correctly indexed when each peak in the diffraction pattern has a label and no expected peaks are missing for the particular structure. By comparing the results with the sequence of ($h^2 + k^2 + l^2$) values, one can determine the Miller indices for the appropriate peaks and the Bravais lattice using the sequence of allowed reflections for cubic lattices or the sequence of allowed peaks expressed in terms of the quadratic form of the Miller indices (Kamwaya et al., 2002).

The following formula can be used to determine the lattice parameters: $\sin^2\theta = (h^2 + k^2 + l^2)(\lambda^2 / 4a^2)$

By following the above methods, we can determine the size and shape of the crystals, as shown in Table 3.

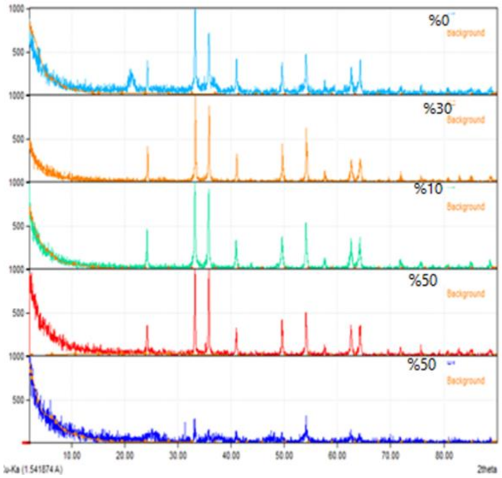

Figure 1: Powder XRD spectra for the sample (3,4,5) and the simulated pattern of FeTiO3

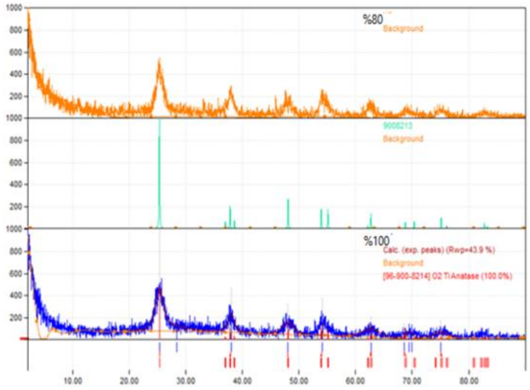

Figure 2: Powder XRD spectra for the sample (1,6) and the simulated pattern of TiO2

Table 3: Size and shape of samples (1-6)

Sample number	Size of crystallite	Shape
1 (100%)	3.11	Tetragonal
2 (0%)	8.17	Trigonal (hexagonal axes)
3 (10%)	7.01	Trigonal (hexagonal axes)
4 (30%)	7.01	Trigonal (hexagonal axes)
5 (50%)	7.01	Trigonal (hexagonal axes)
6 (80%)	2.01	Tetragonal

EDX AND SEM RESULTS

From the EDX results, the amounts of iron and titanium in each sample were calculated, as shown in Table 4.

Table 4: Iron and titanium amounts in samples 1–6.

Ti Content	Fe Content	O Content
1	0	2
0	1	3
0.25	1.47	3
0.03	0.97	3
1	1	3
0.03	0.987	3

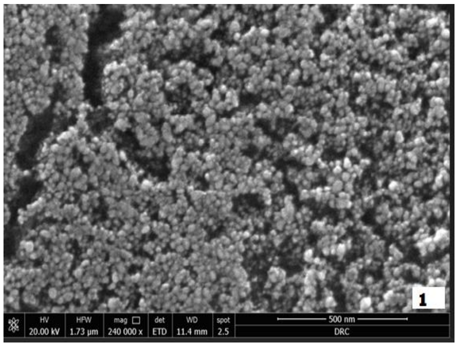

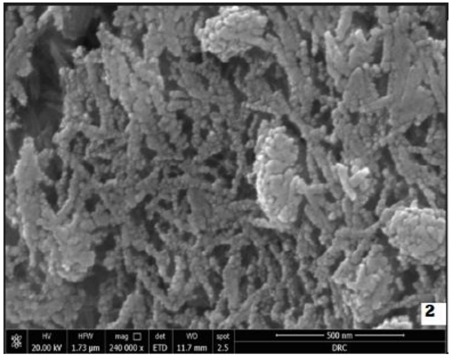

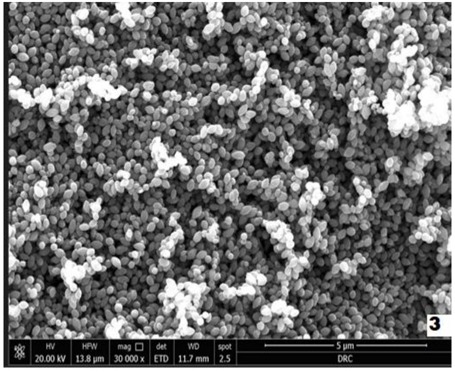

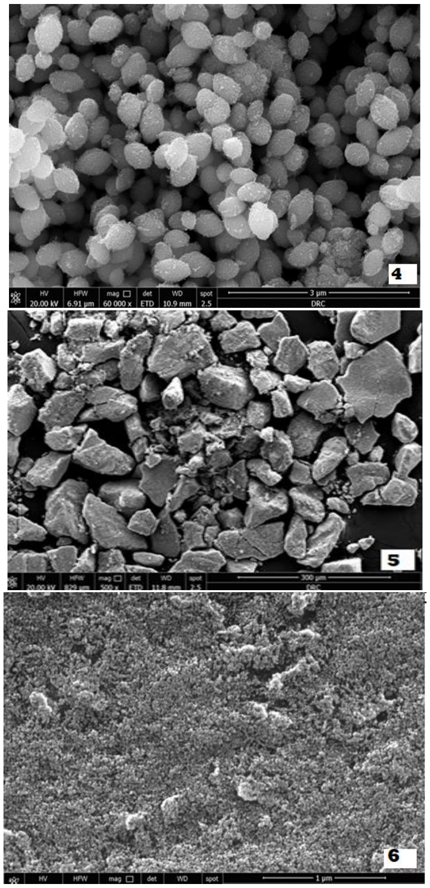

Figure3: Scanning electron microscope (SEM) micro-graph Results for the sample products (1-6).

From the SEM results, the material samples appear to be nano-clusters sized, as shown in Figure 3, which is consistent with the information obtained from the XRD results (Debye-Scherrer's equation calculation).

FT-IR RESULTS

FT-IR is a robust analytical technique used to detect organic materials in the mid-IR and, in some cases, inorganic materials in the far-IR. Figure 4 shows the FT-IR results of the synthesized $FeTiO_3/TiO_2/Fe_2O_3$ nanoparticles. The wide band at 527.67 cm^{-1} is attributed to metal-oxygen bond stretching.

The presence of a broad band at 3450.82 cm^{-1} is consistent with the stretching vibration of surface hydroxyl groups (-OH). A stretching vibration band around 3391.72 cm^{-1} is attributed to both symmetric and asymmetric stretching vibrations of the hydroxyl group (Ti-OH) (Wei et al., 2008). The broad band observed between 3600 and 3000 cm^{-1} corresponds to the OH stretching mode of the hydroxyl group, indicating the presence of moisture in the sample. The characteristic peak at 1627.28 cm^{-1} is related to the O-H bending vibration of absorbed water molecules. Therefore, the two observed peaks at 3391.72 and 1627.28 cm^{-1} correspond to water and a hydroxyl group adsorbed on the surface (Kathiravan et al., 2009).

The sharp peaks centered at approximately 1634 and 1527 cm^{-1} are attributed to the bending vibrations of C=O and NH (Sheta et al., 2022). The bands observed in the low wavenumber range (400–650 cm^{-1}) can be attributed to the vibration of the Ti-O bond in $FeTiO_3$ (Palanisamy et al., 2019). The absorption peaks in the range of 350–500 cm^{-1} are recognized as the Fe-O vibrational bond in $FeTiO_3$ (Ermawati, 2022).

At 470 cm^{-1} and 554 cm^{-1}, distinctive absorption bands (Fe-O bonds) appear in Fe_2O_3 (English et al., 2014). The contributions of anatase titania are represented by the peaks between 463.88 and 728.77 cm^{-1}, and 400 and 800 cm^{-1}. TiO_2 nanoparticles' vibrational absorption of Ti-O-Ti bonds causes the wide absorption band between 450 and 800 cm^{-1} (Lu et al., 2008). This agrees with the XRD results.

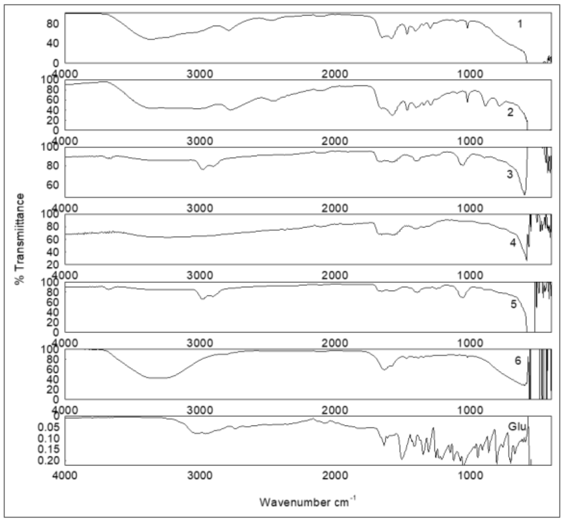

Figure 4: FT-IR pattern of the resulted samples (1-6) and pure glutamic acid

TGA and DTG RESULTS

Fig. 5(A) shows the TG and DTG curves of TiO_2. The weight loss occurs in three temperature regions. The first stage of weight loss, from 45°C to 260°C, is due to the desorption of adsorbed water molecules. The experimentally observed mass loss is 36.38%. The DTG shows an endothermic peak at 100°C. The second stage of weight loss, from 260°C to 400°C, shows a mass loss of 37.02%, attributed to the thermal degradation of organic reagents and surfactants used in the synthetic process. The DTG for this stage shows an endothermic peak at 280°C. The third stage of weight loss, from 400°C to 700°C, is due to the removal of surface hydroxyl groups. The DTG shows two endothermic peaks at 520°C and 680°C (Kil et al., 2015). The total weight loss is 91.83%.

Fig. 5(B) shows the decomposition process in two stages. The first stage starts at 40°C and ends at 280°C. At this stage, DTA shows an endothermic process at 180°C, and a decrease in sample mass is observed (Ru et al., 2014). The first weight loss indicates the evaporation of absorbed water due to the initial decomposition and spontaneous combustion of the complex. H_2O and CO_2 create an oxidizing environment for the combustion of organic components (Guo et al., 2010). The experimentally observed mass loss is 30.08%. The second stage, from 280°C to about 520°C, shows a mass loss of 13.23%, attributed to the combustion of organic products in the finished sample. DTA shows an endothermic peak at 380°C (Lassoued et al., 2017). The total weight loss of this sample is 43.35%.

In samples 3 and 4, the weight loss was approximately 5.84%. This weight loss is related to the removal of adsorbed water. The DTA curve shows endothermic processes at 80°C and 255°C. Upon further heating, a slight weight loss of approximately 1.43% was observed in the temperature range from 270°C to 480°C. This weight loss is mainly due to the thermal degradation of the organic reagents and surfactants used in the synthetic process. No significant weight loss was observed above 480°C, confirming the complete removal of all organic matter from the sample above 480°C and the formation of the pure compound. In the second stage, DTA shows an exothermic process at 470°C (Gupta et al., 2023), as shown in Fig. 5(C and D).

Fig. 5(E) shows that the first part of the TGA curve in this sample shows weight loss below 300°C, which can be associated with the loss of occluded water in the starting material and the combustion of organic material. The experimentally observed mass loss is 8.30%. Furthermore, DTA shows endothermic processes at 75°C and 260°C. The second stage, from 300°C to 700°C, shows a mass loss of 12.52%. DTG shows two exothermic peaks at 460°C and 560°C, which may be related to the crystallization of iron titanate (Morín et al., 2017).

Figure 5(F) shows a weight loss of around 35.49% in the first stage at temperatures between 40°C and 200°C, which is explained by the sample's moisture content being released (Kim et al., 2014). The sample's high moisture content could be due to water molecules absorbed onto the surface during air drying. The DGA for this stage shows exothermic processes at 100°C and 175°C. In the second stage, the observed weight loss of approximately 37.01% in the temperature range of 220°C to 500°C can be ascribed to the disappearance of organic matter bound to the surface or capping molecules, which changes into carbonaceous material. DTA data reveals endothermic peaks at 230°C, 320°C, and 420°C, caused by trapped organic matter slowly breaking down and becoming carbonaceous (Kashale et al., 2016). An exothermic peak event at 680°C is associated with the transition from the anatase to the rutile phase. The varied nanoparticle sizes could be the cause of this broad phase change (Viana et al., 2010)

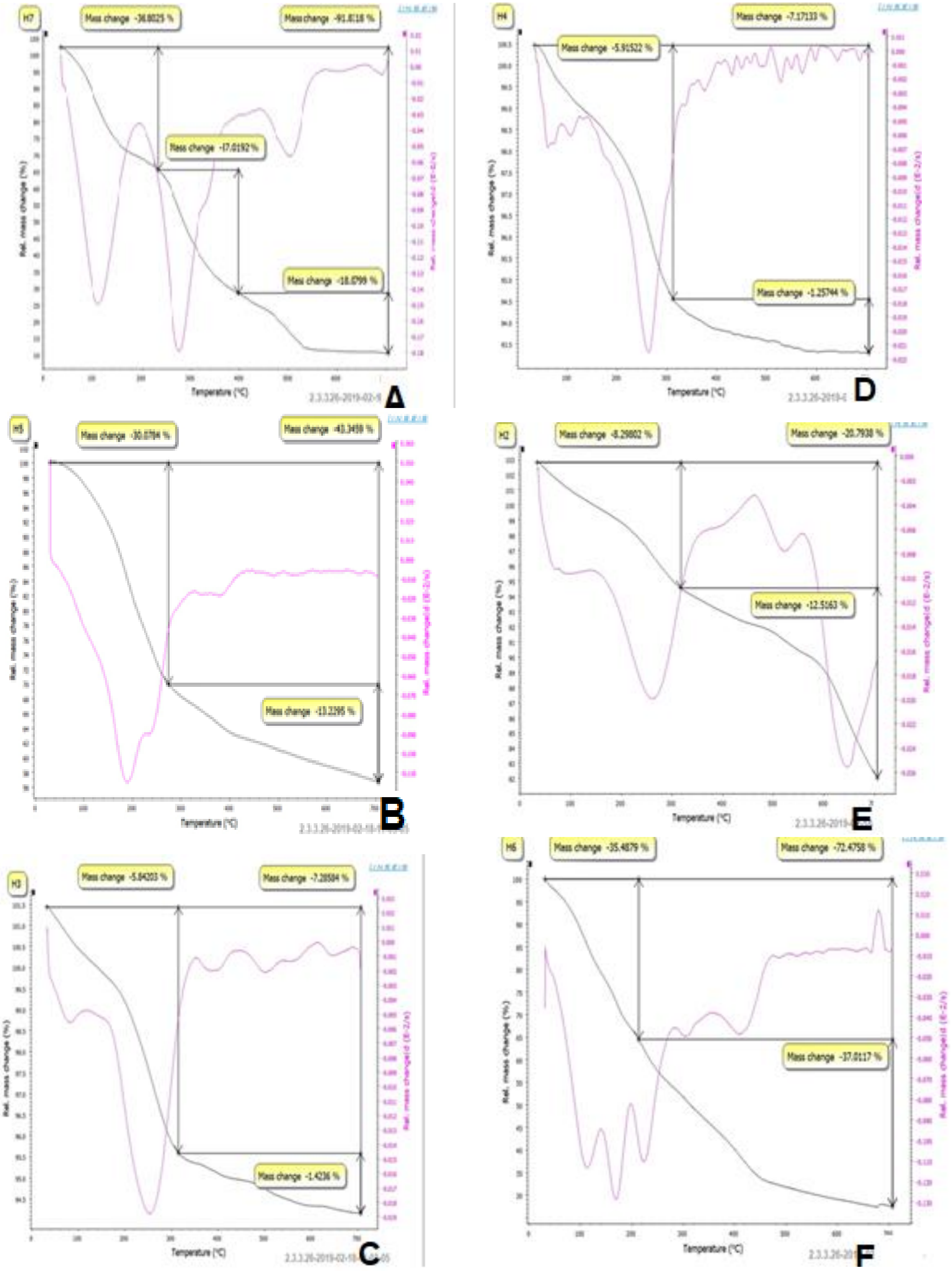

Figure 5: TGA and DTG Results of samples (1-6)

UV-VIS DIFFUSE REFLECTANCE RESULTS

UV-visible diffuse reflectance spectroscopy (DRS) is a commonly used method to investigate the optical characteristics of solids. From the UV-Vis diffuse reflectance spectra, we determined the band gap value by using the tangent straight line intercept method.

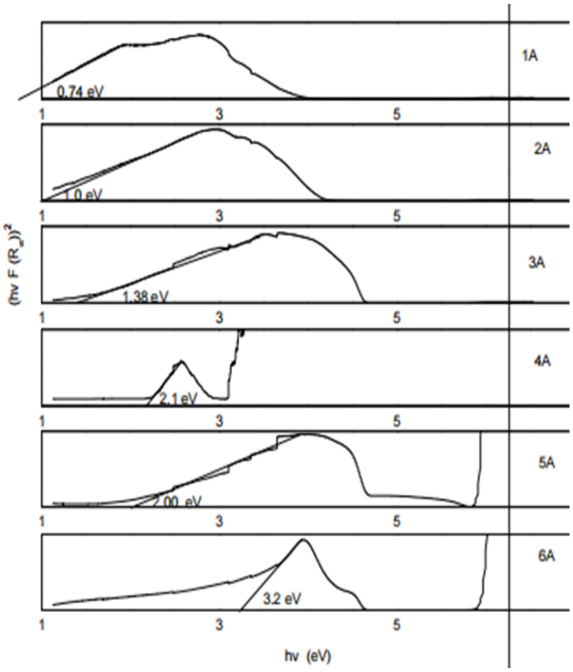

Figure 6: Band gap values of the resulted samples (1-6)

Table 5: Band gap values of the samples (1-6)

Sample NO	Band gap values/Ev
Sample 1	3.14
Sample 2	2
Sample 3	1.38
Sample 4	2.1
Sample 5	1 ev
Sample 6	3.2ev

We can conclude that all the samples, as shown in Figure 6, are semiconductors because they have a band gap of less than 4 eV as shown in table 5.

CONCLUSION

In the initial chapter of this thesis, we provided an introduction to nanotechnology and discussed various methods for its preparation. The thesis specifically focuses on the solvothermal method. The first section includes a literature review that highlights the synthesis methods of iron-titanium nanoparticles (NPs).

The proportions of the two elements with GLU varied across the six samples. After being autoclaved in an oven set to 120°C for 24 hours, the samples were filtered and dried at 38°C.

We employed six distinct spectroscopic analytical methods (XRD, EDX, SEM, FT-IR, TGA, and UV-VIS Diffuse Reflectance) to characterize the products.

Overall, this study demonstrated that samples of TiO_2, Fe_2O_3, and $FeTiO_3$ confirmed the XRD results. The findings showed that a pure cubic phase (FCC) had formed. The average crystallite size of these samples, determined from the XRD data, ranges from 2 to 8 nm. The EDX results are consistent with the XRD findings. SEM confirmed the XRD results, showing that most of the samples were nanoparticles.

The FT-IR results corroborate the XRD conclusions and show that the wide band at 527.67 cm^{-1} is attributed to metal-oxygen bond stretching, present in every sample. Thermal analysis revealed multiple stages of decomposition, and all the samples were thermally stable up to 350°C.

From the UV-VIS data, we conclude that sample No. 1 and 6 have a band gap greater than 3 eV ($Eg > 3$ eV), while all the other samples are semiconductors, with a band gap smaller than 3 eV ($Eg < 3$ eV).

REFERENCES :

1. Abdel-Rahman, L. H., Abu-Dief, A. M., Ismail, N. M., & Ismael, M. (2017). Synthesis, characterization, and biological activity of new mixed ligand transition metal complexes of glutamine, glutaric, and glutamic acid with nitrogen based ligands. Inorganic and Nano-Metal Chemistry, 47(3), 467-480.
2. Carp, O., Huisman, C. L., & Reller, A. (2004). Photoinduced reactivity of titanium dioxide. Progress in solid state chemistry, 32(1-2), 33-177.
3. English, N. J., Rahman, M., Wadnerkar, N., & MacElroy, J. M. D. (2014). Photo-active and dynamical properties of hematite (Fe 2

O 3)–water interfaces: an experimental and theoretical study. Physical Chemistry Chemical Physics, 16(28), 14445-14454.

4. Ermawati, F. U. (2022, December). Phase Formation, Structural, and Microstructural Characterizations of Ilmenite FeTiO3 Nanopowder Prepared from Liquid-Mixing Method. In Journal of Physics: Conference Series (Vol. 2392, No. 1, p. 012022). IOP Publishing.
5. Guo, L., Shen, X., Meng, X., & Feng, Y. (2010). Effect of Sm3+ ions doping on structure and magnetic properties of nanocrystalline NiFe2O4 fibers. Journal of Alloys and Compounds, 490(1-2), 301-306.
6. Gupta, N., Sarkar, A., Pradhan, B., & Biswas, S. K. (2023). Hydrothermal Synthesis of Mesoporous FeTiO3 for Photo-Fenton Degradation of Organic Pollutants and Fluoride Adsorption. Engineering Proceedings, 59(1), 134.
7. He, C., Sasaki, T., Shimizu, Y., & Koshizaki, N. (2008). Synthesis of ZnO nanoparticles using nanosecond pulsed laser ablation in aqueous media and their self-assembly towards spindle-like ZnO aggregates. Applied Surface Science, 254(7), 2196-2202
8. Hussain, M., Alanazi, M. M., Abdelmohsen, S. A., Alahmari, S. D., Abdullah, M., Aman, S., ... & Farid, H. M. T. (2024). Hydrothermal synthesis of Nd-doped FeTiO3 perovskite electrode for enhanced energy storage applications. Journal of Energy Storage, 84, 110920.
9. Kamwaya, M. E. (2002). A simple method for indexing powder diffraction patterns of cubic materials:(1) using the θ-values of reference. Tanzania Journal of Science, 28(1), 1-5.
10. Kashale, A. A., Gattu, K. P., Ghule, K., Ingole, V. H., Dhanayat, S., Sharma, R., ... & Ghule, A. V. (2016). Biomediated green synthesis of TiO2 nanoparticles for lithium ion battery application. Composites Part B: Engineering, 99, 297-304.
11. Kathiravan, A., & Renganathan, R. (2009). Photosensitization of colloidal TiO2 nanoparticles with phycocyanin pigment. Journal of colloid and interface science, 335(2), 196-202.
12. Kil, H. S., Jung, Y. J., Moon, J. I., Song, J. H., Lim, D. Y., & Cho, S. B. (2015). Glycothermal synthesis and photocatalytic properties of highly crystallized anatase TiO2 nanoparticles. Journal of Nanoscience and Nanotechnology, 15(8), 6193-6200.
13. Kim, M. C., Lee, Y. W., Kim, S. J., Hwang, B. M., Park, H. C., Hwang, E. T., ... & Park, K. W. (2014). Improved lithium ion behavior properties of tio2@ graphitic-like carbon core@ shell nanostructure. Electrochimica Acta, 147, 241-249.
14. Lassoued, A., Dkhil, B., Gadri, A., & Ammar, S. (2017). Control of the shape and size of iron oxide (α-Fe2O3) nanoparticles synthesized through the chemical precipitation method. Results in physics, 7, 3007-3015.
15. Li, G., Zhang, W., Luo, N., Xue, Z., Hu, Q., Zeng, W., & Xu, J. (2021). Bimetallic nanocrystals: Structure, controllable synthesis and applications in catalysis, energy and sensing. Nanomaterials, 11(8), 1926.
16. Liu, Z., He, Y., & Ma, X. (2023). Preparation, Characterization and Drug Delivery Research of γ-Polyglutamic Acid Nanoparticles: A Review. Current Drug Delivery
17. Lu, X., Lv, X., Sun, Z., & Zheng, Y. (2008). Nanocomposites of poly (L-lactide) and surface-grafted TiO2 nanoparticles: Synthesis and characterization. European Polymer Journal, 44(8), 2476-2481
18. Morín, M. E. Z., Torres-Martínez, L., Sanchez-Martínez, D., & Gómez-Solís, C. (2017). Photocatalytic performance of titanates with formula MTiO 3 (M= Fe, Ni, and Co) synthesized by solvo-combustion method. Materials Research, 20, 1322-1331.
19. Palanisamy, S., Srinivasan, S., Shyma, A. P., Rajendhran, N., Subramani, K., Murugan, V., & Venkatachalam, R. (2019).

Influence of nanoflower FeTiO 3 in carbon dioxide reduction. SN Applied Sciences, 1, 1-10.

20. Praveen, P., Viruthagiri, G., Mugundan, S., & Shanmugam, N. (2014). Structural, optical and morphological analyses of pristine titanium di-oxide nanoparticles–Synthesized via sol–gel route. Spectrochimica Acta Part A: Molecular and Biomolecular Spectroscopy, 117, 622-629.
21. Ru, J., Hua, Y., Xu, C., Li, J., Li, Y., Wang, D., ... & Zhou, Z. (2014). Microwave-assisted preparation of submicron-sized FeTiO3 powders. Ceramics International, 40(5), 6799-6805.
22. Sheta, S. M., Salem, S. R., & El-Sheikh, S. M. (2022). A novel Iron (III)-based MOF: Synthesis, characterization, biological, and antimicrobial activity study. Journal of Materials Research, 37(14), 2356-2367.
23. Viana, M. M., Soares, V. F., & Mohallem, N. D. S. (2010). Synthesis and characterization of TiO2 nanoparticles. Ceramics International, 36(7), 2047-2053.
24. Wei, J., Zhao, L., Peng, S., Shi, J., Liu, Z., & Wen, W. (2008). Wettability of urea-doped TiO 2 nanoparticles and their high electrorheological effects. Journal of sol-gel science and technology, 47, 311-315.